Characterization of a low-power Cylindrical Hall Thruster

IEPC-2022-359

Presented at the 37th International Electric Propulsion Conference
Massachusetts Institute of Technology, Cambridge, MA, USA
June 19-23, 2022

Tatiana Perrotin[1]
Equipo de Propulsión Espacial y Plasmas (EP2), Bioengineering and Aerospace Engineering department, Universidad Carlos III de Madrid, Avenida de la Universidad 30, 28911 Leganés, Spain

Alfio E. Vinci[2] and Stéphane Mazouffre[3]
Institut de Combustion, Aerothermique, Reactivité et Environnement (ICARE), Centre National de la Recherche Scientifique, 1C Avenue de la Recherche Scientifique, 45071 Orléans, France

Jaume Navarro-Cavallé[4], Pablo Fajardo[5] and Eduardo Ahedo[6]
Equipo de Propulsión Espacial y Plasmas (EP2), Bioengineering and Aerospace Engineering department, Universidad Carlos III de Madrid, Avenida de la Universidad 30, 28911 Leganés, Spain

A fully Cylindrical Hall Thruster prototype was tested in the power range of 30 - 300 W with the objective of understanding the behavior of the discharge as a function of the input parameters. Multiple operating conditions were compared, including two magnetic field configurations, a set of propellant mass flow rates and a range of discharge voltages. The plasma properties were measured in the far-field at various angles and distances, with a Langmuir Probe, a Retarding Potential Analyzer and a Faraday Cup. The discharge current oscillations were analyzed as well, revealing changes in the frequency spectrum due to the voltage and mass flow rate. The experimental results showed that the mass flow rate affected the ionization and, consequently, other related properties such as the plasma density, currents, and propellant utilization. The discharge voltage also appeared to influence the measured variables, in particular the ion energy and propellant utilization.

I. Nomenclature

ε_0	=	vacuum permittivity
k_B	=	Boltzmann constant
q	=	elementary charge
α	=	beam half-angle
γ	=	polytropic index
η_{cur}	=	current utilization efficiency
η_{div}	=	divergence efficiency
η_u	=	propellant utilization efficiency
θ	=	probe angle with thruster axis
λ_D	=	Debye length
ν	=	collision frequency

[1]PhD student, tperroti@pa.uc3m.es
[2]PhD student, alfio.vinci@cnrs-orleans.fr
[3]Research Director, Head of electric propulsion team, stephane.mazouffre@cnrs-orleans.fr
[4]Assistant Professor, janavarr@ing.uc3m.es
[5]Professor, pfajardo@ing.uc3m.es
[6]Professor, Head of EP2 team, eahedo@ing.uc3m.es

$\mathcal{E}_i$ = ion energy
$\rho_{L,e}$ = electron gyroradius
ϕ_{fl} = floating potential
ϕ_{pl} = plasma potential
A_p = probe surface area
$\vec{B}$ = magnetic field
I_{BC} = back coil current
I_{TC} = top coil current
I_e = electron current
I_i = ion current
$I_{i,z}$ = axial ion current
j_i = ion current density
$\dot{m}_a$ = anode mass flow rate
$\dot{m}_c$ = cathode mass flow rate
m_e = electron mass
m_i = ion mass
n_e = electron density
P_d = thruster discharge power
P_h = cathode heating power
r = radial distance to exit plane
r_p = probe radius
T_e = electron temperature
V_B = probe voltage bias
z = axial distance to exit plane

II. Introduction

As space actors seek more and more solutions for large-scale and short-lifetime missions, new propulsion systems must be developed to provide maneuverability even when the power and mass budgets are tightly restricted. Hall Effect Thrusters (HET) have proven to suit said needs over multiple decades and the thrust they provide makes them particularly interesting, compared to other electric thrusters, for these new mission design challenges. Although this technology is quite mature for medium and high power thrusters, more development is required for few sub-kilowatt HET to achieve satisfactory performance and lifetime.

The Cylindrical Hall Thruster (CHT) was introduced in [1] as an alternative to the traditional annular HET. This device still relies on a closed $\vec{E} \times \vec{B}$ electron drift but the central pole is removed in an attempt to reduce power losses and erosion of the ceramic wall. Such a change of geometry also simplifies the mechanical design, thermal management and generation of the magnetic field, which are major issues that arise when scaling plasma thrusters to low electric power. This work summarizes the characterization of a 200 W CHT prototype through measurements of the plasma properties in the plume and of the discharge parameters. Multiple research teams have carried out experimental investigations on low power CHT over the past two decades. Similar intrusive diagnostics were used to map the plasma properties, with a focus on the internal discharge rather than the plume [2–9]. These works described testing of a broad range of thruster designs in terms of channel geometry, topology of the magnetic field and operating conditions, with the objective of doing parametric study to enhance the thruster design and operation.

The device and testing conditions are described in section III, after, the thruster ignition, operation and mechanical behavior are described in section IV. Then, far-field measurements of the electron temperature, plasma density and plasma potential with a Langmuir Probe (LP) are reported in section V.A. Subsequently, sections V.B and V.C describe the results of ion energy and current in the beam, obtained respectively with a Retarding Potential Analyzer (RPA) and a Faraday Cup (FC). Eventually, the discharge oscillations are analyzed in section V.D using data acquired with a Current Probe (CP).

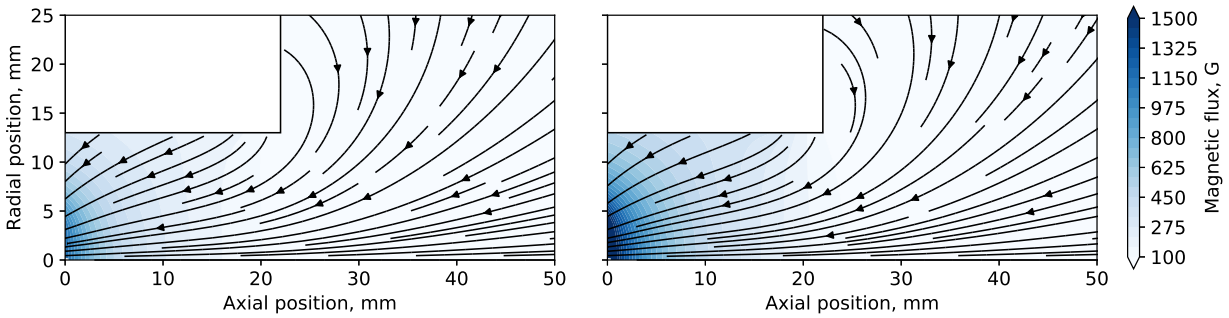

(a) I_{TC}**=1 A,** I_{BC}**=1.7 A** **(b)** I_{TC}**=2.2 A,** I_{BC}**=2.5 A**

Fig. 1 Magnetic flux and streamlines in the CHT channel for two different configurations of coils currents, from simulations

III. Experimental set-up

A. Thruster and cathode

The thruster used in this work is a CHT designed to operate around 100 - 300 W of discharge power. It is made of a 22 mm-long, 13 mm-radius cylindrical boron nitride channel similar to the one described in [2, 10]. The thruster does not have any coaxial region, thus the upstream wall of the discharge chamber ends flush with the annular copper anode. The latter possesses six holes for propellant injection that are evenly distributed in the azimuthal direction in order to optimize ionization and plume symmetry [6]. Figure 1a shows the default magnetic field $\vec{B}$ that is generated by two coils powered in direct configuration. This is meant to limit the beam divergence and large electron flux to the wall that can be observed with a cusped field [11, 12]. The field is shaped by the soft iron components of the thruster, which are the casing and an internal central pole placed in the back coil and covered by the back wall of the channel. Figure 1b displays the magnetic topology obtained with a different set of currents in the coils, that results in a flux with a larger magnitude and a larger ratio of axial-to-radial flux compared to the reference field. A more detailed description of the thruster is available in [13].

The thruster was paired with a MIREA-type thermionic cathode made of a LaB_6 pellet-shaped emitter [14]. It was positioned in such a way that the keeper orifice was 50 mm away from the thruster axis, vertically, and 34 mm downstream the exit plane, with the cathode axis orthogonal to the thruster axis. The cathode position relative to the thruster is showed in Fig. 2. Since this neutralizer is sized to deliver 5 A of current, the anode discharge current was not sufficient for it to be self-heated. As a consequence, 60 to 80 W were supplied to the heater during thruster operation. Instead, the keeper was used only during ignition and was kept floating afterwards. The heating power was tuned as the cathode showed increasing difficulty to sustain the discharge over time, likely because of material deposition on the emitter surface and heater ageing. This translated into an evolution of the relation between the heating power, discharge power and Cathode Reference Potential (CRP). When necessary, the heating was adjusted to have the desired CRP. The mass flow rates of research-grade xenon fed to the anode and to the cathode were set independently with two Alicat MC-series Mass Gas Flow Controllers, calibrated for this propellant. All the tests were performed with a cathode flow rate of 2 sccm. The anode and keeper circuits each included a parallel RLC filter that was meant to protect the DC power supply from the discharge oscillations ($R = 100\Omega$, $C = 8\mu F$, $L = 300\mu H$).

B. Test facility

The experiments presented hereafter were performed in the New Experiment on Electric Thrusters (NExET) vacuum chamber which consists of a 1.8 m-long, 0.8 m-diameter stainless steel cylindrical vessel. The facility is equipped with a primary pump, a turbomolecular pump and a cryogenic panel cooled down to approximately 40 K. This allows for reaching a base pressure in the order of 10^{-7} mbar. During the tests, the chamber pressure was maintained below 3×10^{-5} mbar whenever the total xenon mass flow rate was under 7 sccm. The vacuum chamber was grounded electrically, and the structure supporting the thruster, cathode, and probes, was fixed to it mechanically. The probes

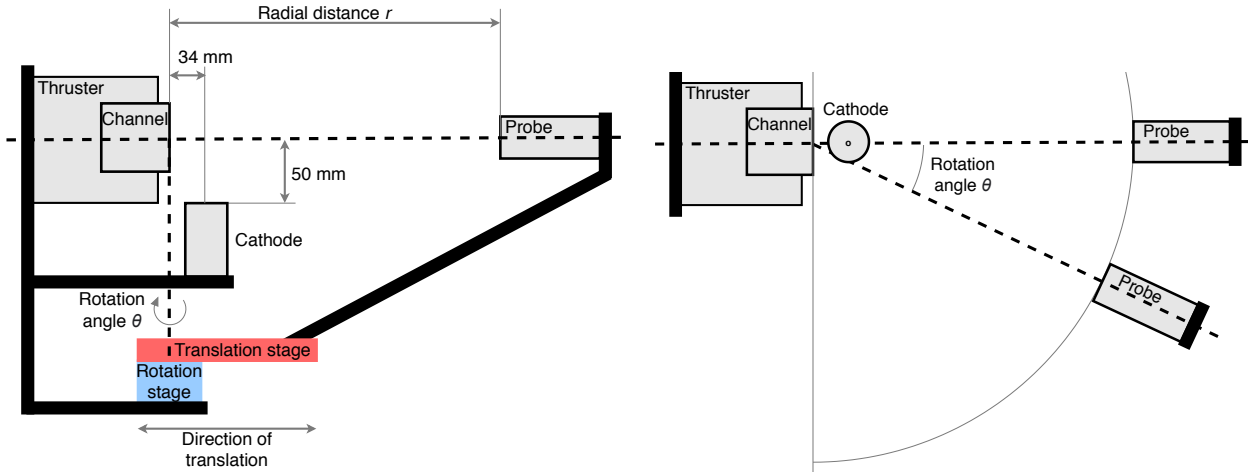

Fig. 2 Schematic of the experimental set-up used for polar probe scans in the thruster plume, side view (left) and top view (right)

were installed on an arm connected to a 15 cm-range translation stage, itself mounted on a rotation stage and each of them was controlled independently. The rotation axis was contained in the exit plane and intersecting the axis of symmetry of the thruster, as represented in Fig. 2. The probes were oriented in the radial direction. The temperature of the electromagnet, thruster casing and cathode flange was monitored using K-type thermocouples.

C. Probes description and theory

1. Langmuir Probe

The current-voltage characteristic of a simple conductor immersed in a DC discharge plasma can be used to determine several of its local properties such as the electric potential, plasma density, and electron temperature and energy distribution function. Langmuir Probe measurements were thus used to characterize the spatial variation of these properties in the plume of the CHT, under different operating conditions. The main objective was to better understand the behavior of the plasma particles in the beam, while future investigations shall compare these experimental data with hybrid PIC/fluid simulations and contribute to improving the models used.
The probe used for this test campaign had a 7.3 mm-long, 0.6 mm-diameter cylindrical tip inserted into alumina tubes. It was electrically biased with respect to the vacuum chamber using a remotely controlled Keithley 2410 Source Measurement Unit (SMU), that also had the function of measuring the current collected by the LP as the voltage was swept from -70 V to 20 V. In order to compute the main plasma properties from the raw current-voltage characteristic of the LP, the method described by [15] is employed. Orbital Motion Limited (OML) theory estimates that the saturated ion current I_i should be approximately proportional to the square root of the probe voltage bias. Hence, the ion current was evaluated with $I^2 \propto V_B$ using a linear fit on the negative part of the current, which gave matching results although the sheath regime was often transitional rather than OML (as per the value of the r_p/λ_D ratio). From OML theory, Eq. (1) describes the expression of the ion current for a probe biased below plasma potential.

$$I_i = A_p n_e q \frac{\sqrt{2}}{\pi} \left(\frac{q\left(\phi_{pl} - V_B\right)}{m_i} \right)^{1/2} \tag{1}$$

From this relation, the plasma density was deduced with Eq. (2) using the slope of the $I^2 - V_B$ curve.

$$n_e = \left(\frac{-d(I^2)}{dV_B} \frac{\pi^2 m_i}{2A_p^2 q^3} \right)^{1/2} \tag{2}$$

The electron current I_e was then calculated by subtracting I_i to the raw probe current. The plasma potential ϕ_{pl} was deduced from the inflection of I_e, given by the maximum of its derivative dI_e/dV_B. For Maxwellian plasma electrons,

I_e is an exponential function of $q(V_B - \phi_{pl})/k_B T_e$ in the electron retarding part of the I-V curve, i.e. between floating and plasma potential. This relation allows for determining the electron temperature T_e by fitting a line to the plot $\log(I_e) - V_B$ and finding the inverse of its slope. In practice, the range of voltages used for this fit had to be adjusted since the linearity of $\log(I_e)$ was altered at low biases, which lead to large uncertainties. This is attributed to the non-negligible depletion of the high-energy tail of the electron energy distribution function (EEDF) in comparison with a Maxwellian distribution. The EEDF was estimated from the second derivative of I_e, with the Druyvesteyn method as described in [16]. This allowed for verifying the presence of such a tail depletion, but the curves obtained are not presented since they systematically showed distortions that were ascribed to the measurement conditions, and the data were too noisy to provide a reliable second derivative of the current. Note that the values of T_e and n_e provided in this document are the ones computed as described hereinabove and not the ones given by the moments of the EEDF.
It is important to specify that all the current-voltage characteristics obtained with the LP were smoothed using a locally weighted smoothing algorithm and the results computed were affected by the chosen parameters, particularly the values taken by the plasma potential, electron temperature, and consequently the polytropic index. The amount of smoothing was selected to be sufficient but minimal.

2. Retarding Potential Analyzer

The RPA used in this experiment had a diameter of 26 mm and was composed of four 0.1 mm-thick grids, spaced by 0.2 mm-thick insulators. The grids had 0.15 mm-diameter holes and 25 % transparency. The probe was controlled with a Semion Impedans, Ltd through the dedicated software in order to set the voltage of the grids independently, since each of them acts as an energy discriminator for the plasma particles. The purpose of the second grid is to prevent plasma electrons from penetrating inside the probe, while the fourth one ensures the recollection of secondary electrons from ion impact. Ideally, only the ions with an energy larger than the third grid (filter) voltage can reach the collector and contribute to the current measured. This principle allows for reconstructing the shape of the ion energy distribution function (IEDF). The magnitude measured is the total ion energy in the direction of the probe, $\mathcal{E}_i$. Knowing the local plasma potential, one can use Eq. (3) to distinguish the potential and kinetic energies derived from the total energy conservation, and obtain v_i, the velocity of the ions in the plasma before they enter the sheath that forms in front of the RPA [17].

$$\mathcal{E}_i = \frac{1}{2} m_i v_i^2 + q\phi_{pl} \tag{3}$$

For the entirety of this experiment, the first grid was kept at floating potential and the collector at -1 V. In the majority of cases, the plasma electron repeller and secondary electron repeller were biased at -30 V and -60 V, respectively, but these voltages were adjusted when necessary to counter distortions of the collected current curve. The ion filter grid was swept from 0 V to 400 V in steps of 0.5 V. The vacuum tank was taken as potential reference for those biases.
Each I-V curve, which relates the collector current to the ion filter voltage, is the average of two consecutive sweeps. The outcome is processed with a locally weighted smoothing algorithm and then differentiated. As the IEDF is proportional to the derivative of the ion current, the shape of $-dI/dV$ is later on referred to as the IEDF [18].

3. Faraday Cup

This experiment included measurements of the ion current density in the beam using a Faraday Cup. This device allows for collecting ions and repelling electrons in order to measure the ion current accurately in the beam. The collimator defines the solid angle of ion collection. The cup shape cancels sheath effects and ensures secondary electrons recollection. The probe used in these tests was composed of a graphite collimator electrode exposed to the plasma, with an aperture diameter of 10 mm. For all the measurements, the collimator was left floating. The collector was made of a 40 mm-long cylinder and a 10 mm-diameter porous aluminum disk. It was biased at -40 V. The housing of the FC was kept floating, and all the inner and outer parts of the probe were insulated from the others with PEEK material. Some elements about the probe design and the selection of the materials can be found in [19].
The current density j_i is computed by dividing the collected current by the aperture area A_p = 78.5 mm^2. Then the total ion current in the beam I_i is computed assuming an axisymmetric beam and integrating j_i over the hemispherical surface of radius r, which is the distance between the exit plane and the probe entrance, as in Eq. 4 [20, 21].

$$I_i = \pi r^2 \int_{-\pi/2}^{\pi/2} j_i(\theta) |\sin(\theta)| \, d\theta \tag{4}$$

Note that the FC scans are done at a distance r greater than ten thruster diameters. Since this is the far-field, the thruster can be considered a point source, which is why the correction factors suggested in [20] are not used. The validity of this assumption was checked by comparing the results computed with and without using the correction factors, that turned out to be almost identical.
The axial ion current $I_{i,z}$ is then obtained with Eq. 5 and is used to compute the beam half-angle, which is $\alpha = \cos^{-1}(I_{i,z}/I_i)$ for far-field measurements.

$$I_{i,z} = \pi r^2 \int_{-\pi/2}^{\pi/2} j_i(\theta) \cos(\theta) |\sin(\theta)| \, d\theta \tag{5}$$

From these magnitudes, three partial efficiencies can be estimated: the current utilization $\eta_{cur} = I_i/I_d$, the propellant utilization $\eta_u = I_i m_i/(q(\dot{m}_a + \dot{m}_c))$ and the divergence efficiency $\eta_{div} = \cos^2(\alpha)$.

4. Current Probe

The discharge current was monitored using a Teledyne LeCroy CP031A current probe clamped to the anode electrical cable on the atmospheric side of the circuit, and connected to a Teledyne LeCroy oscilloscope. This probe has a frequency bandwidth ranging from DC to 100 MHz. The data were acquired at a sampling rate of 2.5 MHz. The Power Spectral Density (PSD) was computed from the time signal using Welch's method.

IV. Thruster operation

A. Ignition

Once the required conditions for ignition were determined, the same procedure was followed to ensure repeatability and highlight any changes of behavior of the thruster or the cathode. The heating power of the cathode was ramped-up at a rate of 2 A/min up to 8 A, while propellant was flowing in the device. When reaching this point, a voltage bias was applied to the keeper to turn on the keeper discharge with a current limited to 0.7 A. Then, the mass flows of the cathode and the anode were set to 2 sccm and 3.5 sccm, respectively. The anode was biased to 550 V with respect to the cathode and the thruster coils current were set to the default values (Fig. 1a). The cathode heating power ramp-up was then carried on until anode discharge ignition, usually above P_h = 300 W. Immediately after ignition, the anode bias was set to 300 V and after a few minutes, the keeper discharge was switched off and the heating power was gradually decreased to 60 - 80 W. Once the thruster and cathode operated steadily, the discharge conditions were tuned for the tests.
For all the operating points mentioned throughout this work, the main discharge was controlled in voltage. Current saturation of the discharge was a major issue in past experiments with this thruster when coupled with other cathodes. This seemed to be mainly caused by a too large cathode mass flow rate and/or a too large cathode temperature, both resulting in an excess of thermionic current, for a given anode voltage bias.

B. Effects of design on operation

Some phenomena worth mentioning were observed during thruster ignition, operation, and visual inspection after the tests, they are reported hereafter. The first noticeable thing was the visual aspect of the gas injection, which seemed very asymmetrical and uneven during ignition, as one can see in Fig. 3 (left). This picture displays the thruster in the first few minutes of ignition, characterized by a low anode current ($O(10^{-2})$ A) slowly increasing. However, after a stable discharge was established, the six injectors appeared to be used rather homogeneously, as showed in Fig. 3 (right). In addition, despite the effort done in the mechanical design and materials selection to protect the coils from overheating, the one placed closest to the channel underwent large thermal fluxes due to the power losses from the plasma. Uninterrupted firing was limited to 30 - 60 minutes by the 210 °C rating of the enamel, depending on the operating point. The thruster was allowed to cool down for about an hour after each test. These observations suggest that the thermal management and the gas injection system can be improved in the next design iteration.
After the test campaign during which the thruster fired under a hundred hours, it was observed that the ceramic wall covering the central magnetic pole was eroded on a small circular surface (Fig. 4), with a depth of about half a millimeter,

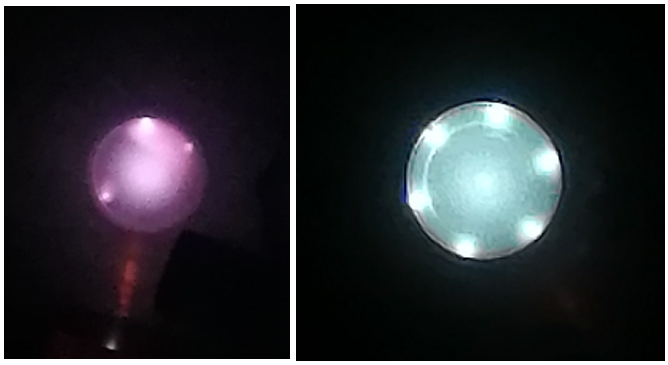

Fig. 3 Injector during ignition (left) and operation (right)

Fig. 4 Eroded central ceramic

i.e. 25 % of the wall thickness. In this region, the magnetic field lines intersect the wall perpendicularly and the plasma is particularly dense on the thruster axis due to the converging electric field in the channel, therefore exposing the ceramic to large energy fluxes from the plasma particles. Wall material sputtered at this location in a CHT was observed by [22], after a short firing time.

V. Results from plasma diagnostics

A. Langmuir probe

1. Plasma potential, electron temperature and density

The thruster operating conditions taken as a reference in this work are the following: V_d = 300 V, $\dot{m}_a$ = 3.5 sccm, I_{TC} = 1 A, I_{BC} = 1.7 A. For this test point, the plasma properties in the plume were scanned over the ranges r = 5 to 20 cm and θ = 0 to 80 °. The results are depicted in Fig. 5. The half cross-section of the discharge chamber is represented by solid lines, each measured location is indicated by a black dot, and the map is obtained by two-dimensional cubic interpolation.

Figure 5 shows reasonable plasma behavior for a 200 W CHT plume. The trends visible in the plasma properties are also in general agreement with other published work on HET [23, 24]. While the plasma density (Fig. 5, center) decays smoothly in both axial and radial directions, the electron temperature (Fig. 5, left) and plasma potential (Fig. 5, right) show some radial gradients near the thruster that could be the consequence of the peculiar converging beam created by the axial magnetic field component in the CHT. The values of plasma potential also show that the voltage drop after z = 5 cm is small with respect to the discharge voltage, thus the ions are likely almost fully accelerated at this distance from the exit plane.

The uncertainty on the density is large but the values reported by [25] are smaller for a chamber pressure one order of magnitude lower, and very similar test conditions in terms of thruster design, discharge voltage, anode and cathode mass flow rates, etc. Thus, the vacuum level possibly had some effect on the thruster operation during the tests. Nevertheless, the high plasma densities measured in the CHT plume are quite promising. The variation along the axis of those three plasma parameters is represented in Fig. 6. Four operating conditions were scanned to observe the effect of the discharge voltage, anode mass flow rate, and magnetic field. In each case, a single parameter is varied with respect to the reference conditions. Therefore, the test points are: the reference one V_d = 300 V, $\dot{m}_a$ = 3.5 sccm, I_{TC} = 1 A, I_{BC} = 1.7 A, a lower voltage V_d = 250 V, $\dot{m}_a$ = 3.5 sccm, I_{TC} = 1 A, I_{BC} = 1.7 A, a larger mass flow rate V_d = 300 V, $\dot{m}_a$ = 5 sccm, I_{TC} = 1 A, I_{BC} = 1.7 A, and a stronger magnetic field V_d = 300 V, $\dot{m}_a$ = 3.5 sccm, I_{TC} = 2.2 A, I_{BC} = 2.5 A. Overall, Fig. 6 mainly reveals that the plasma properties are only very mildly modified by the variations in the conditions tested, at the locations measured. One can still notice a few interesting features. With a larger anode mass flow rate $\dot{m}_a$ (cyan), the plasma density is larger than in any other cases. This is likely due to the ionization collisions being enhanced by the larger neutral density. Instead, the potential is slightly larger in the whole plume at 5 sccm, and its axial evolution is mostly altered near the thruster where the effect of the density is most visible. A stronger magnetic field (navy) seems to result in a very moderately larger plasma density on the axis. Finally, reducing the anode voltage bias (red) has no apparent effect on the plasma density but the lower electric field results in colder electrons and a lower potential drop

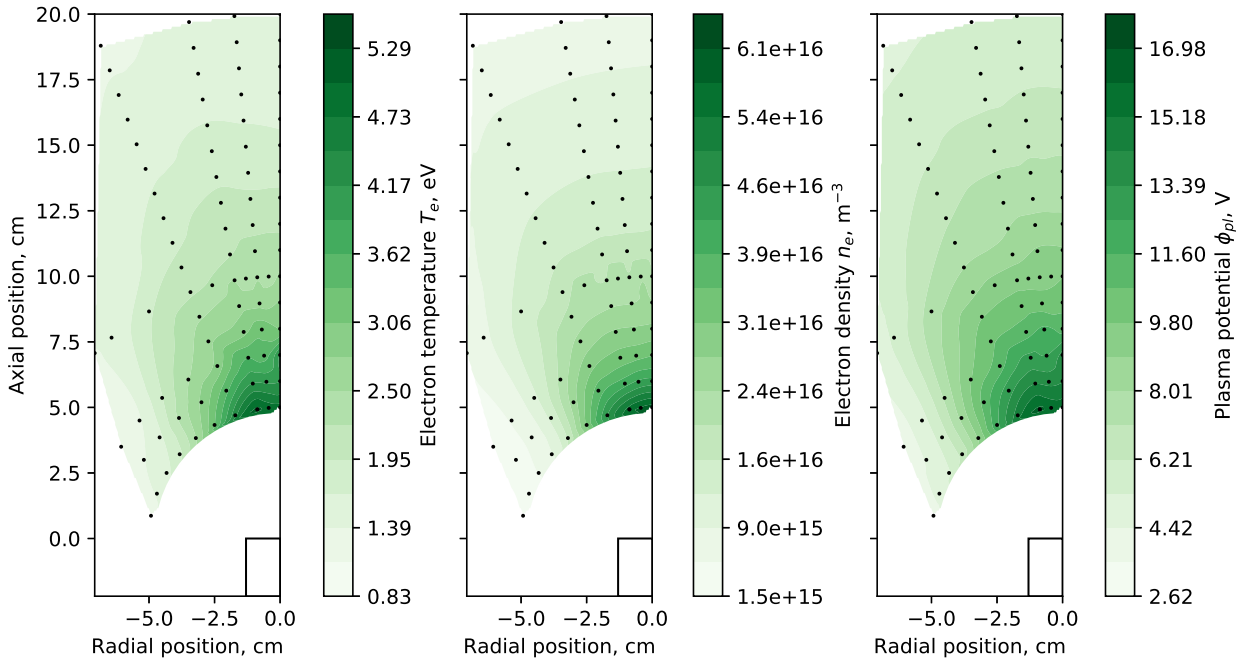

Fig. 5 2D maps of the plasma properties T_e, n_e and ϕ_{pl} measured with the LP in the conditions: I_{TC} = 1 A, I_{BC} = 1.7 A, V_d = 300 V, $\dot{m}_a$ = 3.5 sccm. The black dots represent the locations of the measurements.

Table 1 Polytropic index γ obtained from linear fits in Fig. 7

Operating conditions	γ	γ upstream	γ downstream
Ref.	1.630	1.276	1.646
V_d = 250 V	1.585	1.519	1.563
$\dot{m}_a$ = 5 sccm	1.527	0.789	1.610
I_{TC} = 2.2 A, I_{BC} = 2.5 A	1.644	1.444	1.637

in the upstream part of the probed region. These slight differences between the four operating conditions were also observed with radial scans performed at θ = 10 ° and θ = 20 °.

2. Polytropic index

Knowing the axial variation of the electron temperature and the plasma density from LP measurements, it is possible to evaluate the electron cooling rate using a polytropic relation (Eq. (6)). This can be of particular interest to improve numerical models of electron thermodynamics in expanding plasma plumes.

$$\left(\frac{n_e}{n_{e0}}\right)^{\gamma-1} = \frac{T_e}{T_{e0}} \tag{6}$$

For each of the four thruster operating conditions mentioned in section V.A.1, a plot of $\log(T_e/T_{e0}) - \log(n_e/n_{e0})$ is represented in Fig. 7. A least square regression is used on the experimental results, the curve fitted over the full data-set is showed as a black dashed line. The polytropic index γ is retrieved from the slope of this curve and its value is given in the second column of table 1 for all cases. In all graphs except Fig. 7b, the last few points in the upstream region (corresponding to the right hand-side of the plots in Fig. 7) appear to vary with a different rate compared to the downstream part. This highlights the possibility that the polytropic index is not homogeneous in the plume. For this reason, two other elements are displayed on each graph: a red dashed line is fitted to the three most upstream data points, while a cyan dashed line is fitted to all the remaining downstream points. Although the plots seem to exhibit this index

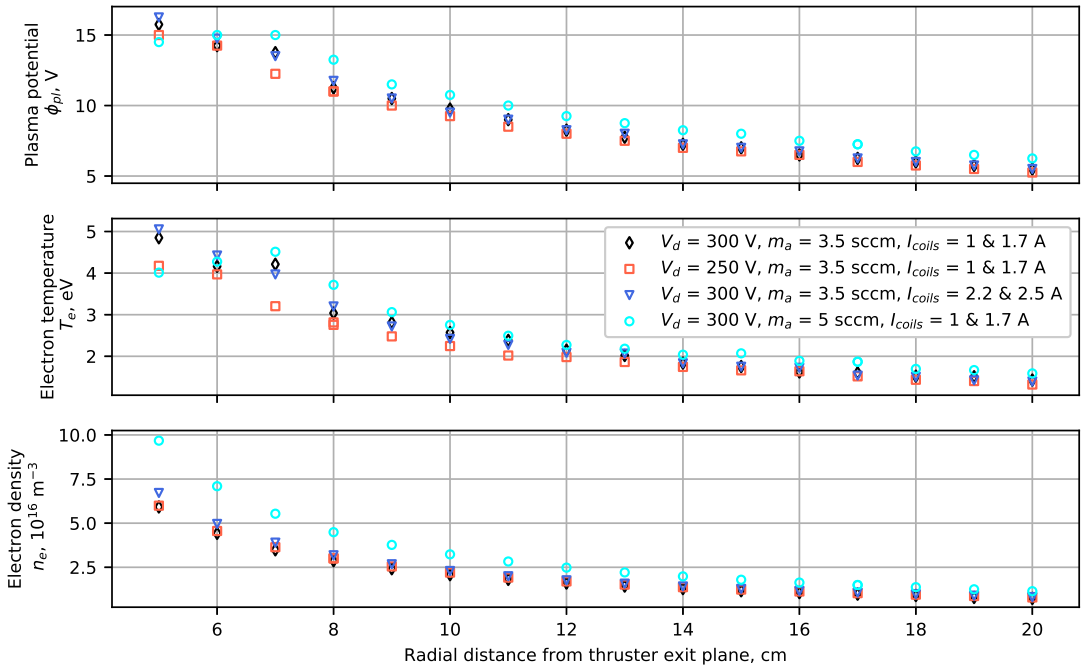

Fig. 6 Variation of plasma properties T_e, n_e and ϕ_{pl} along the thruster axis (θ = 0 °), for four different operating conditions

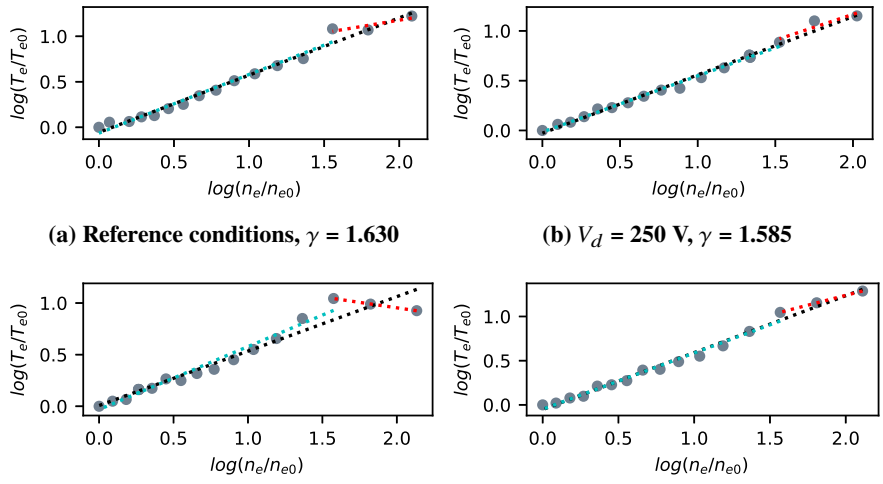

(a) Reference conditions, γ = 1.630 **(b) V_d = 250 V, γ = 1.585**

(c) $\dot{m}_a$ = 5 sccm, γ = 1.527 **(d) I_{TC} = 2.2 A, I_{BC} = 2.5 A, γ = 1.644**

Fig. 7 Logarithmic plot of the relation between normalized electron temperature and density. The dots are experimental data and the dashed lines are least square fits over different ranges. The single parameter that differs from the reference conditions is specified in each individual caption.

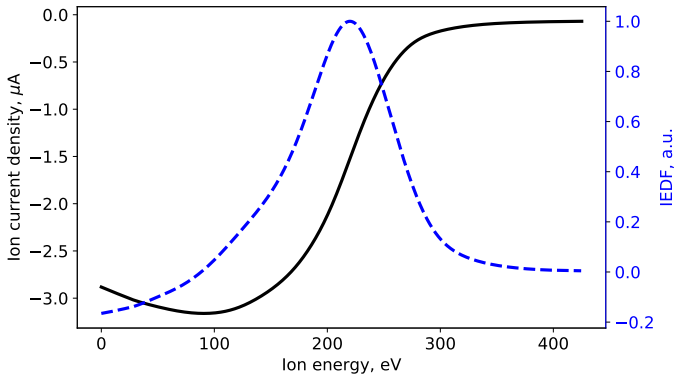

Fig. 8 Collected ion current and IEDF as function of the filter grid voltage bias, at z = 18.5 cm and θ = -30 °, in the reference operating conditions

variation, it is clear that the data span available is limited to get a high confidence fit for the upstream part. The pair of polytropic indices obtained is anyways provided in the third and fourth columns of table 1 for qualitative comparison. In particular, the upstream value of γ in the case $\dot{m}_a$ = 5 sccm seems too small to be physical in the conditions of the plume and this is certainly due to both the uncertainty on the results of T_e and n_e, and the lack of data points to fit. The results presented in this table are significantly higher than the ones reported in other works from measurements in Hall thruster plume, which were between 1.16 and 1.37 [23, 26]. This could be related to the discharge power and anode mass flow rate being one order of magnitude larger for these thrusters compared to the CHT prototype characterized here.
It is noteworthy to mention that γ is lowest in the case of large anode mass flow rate, and the change of slope is more obvious in Fig. 7c than in any other case. This probably ensues from the enhanced collisionality due to the larger densities in these conditions, which affects the degrees of freedom and the thermodynamic state of the plasma [27–29]. In the case of a stronger magnetic field (Fig. 7d), the polytropic index is slightly larger than in the reference conditions. The magnetic field could affect γ through the anisotropy of electron transport properties, but even though $|B|$ has larger values with this topology, it does not seem to be the explanation here since the electrons remain unmagnetized in this region of the plume. The difference with the reference point is most likely related to a change in the collisions undergone by electrons that affect thermalization, like in the previous case. Instead, the polytropic index is decreased when the discharge voltage is reduced from 300 V to 250 V (Fig. 7b). This behavior could be imputed to the different axial and radial components of the electric field, which has been observed to have an impact on γ [30] as it conditions electron diffusion.

B. Retarding Potential Analyzer

As described in section III.C.2, the RPA probe was used to measure the ion energy distribution function locally in the plume, and the most probable ion energy was estimated from the peak of the IEDF. An example of current-voltage curve acquired with the probe is presented as a solid black line in Fig. 8. The derivative of this curve is showed on the same graph as a dashed blue line. Note that the non-monotonic variation of the current at low biases is likely due to electrons altering the collected ion current. This affects the left-hand side of the IEDF as well, which takes non-physical negative values (Fig. 11). Additionally, in the results presented hereafter, the local plasma potential was not measured at the locations probed with the RPA, however, the LP data presented in Fig. 5 and 6 indicate that ϕ_{pl} is lower than 6 V for all operating conditions, at distances greater than 18.5 cm, i.e. for all RPA measurements.
The four thruster operating points compared in section V.A are considered again in Fig. 9a, that displays the variation along the thruster axis of the most probable ion energy, assessed from the peak of the IEDF. As expected from the low plasma potential in the probed region, the ion acceleration beyond z = 18.5 cm is quite insignificant. This is highlighted in Fig. 9a since the energy measured is almost constant over 15 cm. Comparing the reference conditions (black) with the low discharge voltage case (red), one can see that the ion energy in the beam increases with the voltage, which corresponds to the predicted behavior. Increasing the propellant mass flow rate at the anode and using a stronger magnetic field both seem to worsen the acceleration, since the ion energy is lessened in these conditions with respect to the reference ones. Thus, all the parameters varied (V_d, $\dot{m}_a$ and $\vec{B}$) clearly affect the voltage utilization of the thruster.

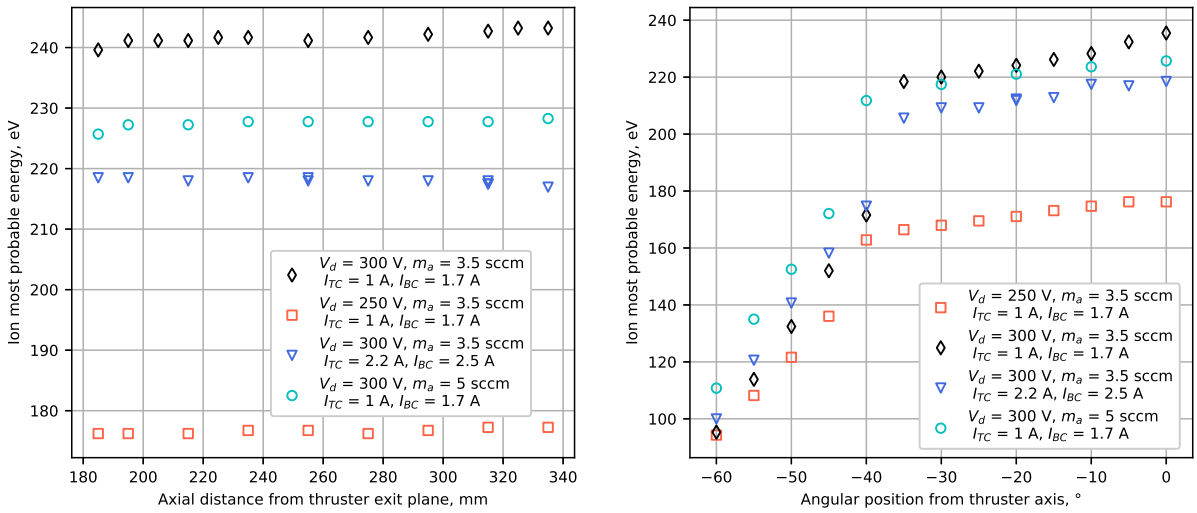

(a) Radial variation at θ = 0 ° **(b) Angular variation at z = 18.5 cm**

Fig. 9 Spatial variation of the most probable ion energy, for four operating conditions

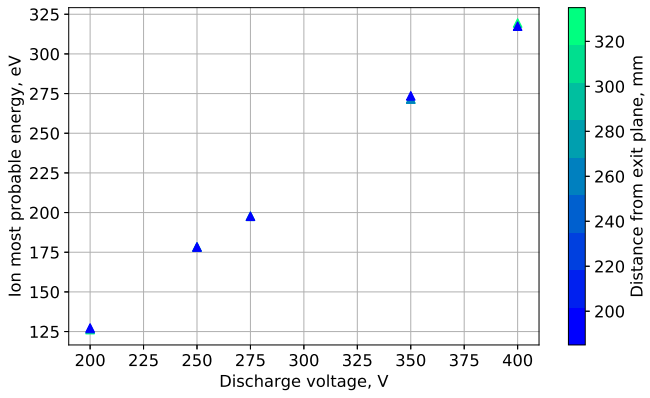

Fig. 10 Variation of the most probable ion energy with the discharge voltage, at three distances from the thruster

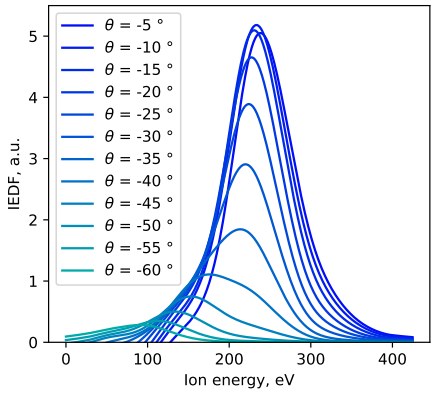

Fig. 11 Evolution of the IEDF with the angle, at z = 18.5 cm, in the conditions: I_{TC} = 1 A, I_{BC} = 1.7 A, V_d = 300 V, $\dot{m}_a$ = 3.5 sccm

Using plasma diagnostics inside the thruster channel would give insight on the relative position of the ionization and acceleration regions, and help understanding the reasons for such a variation.
Angular scans of the ion energy at z = 18.5 cm are visible in Fig. 9b. The previous conclusions can be observed on this plot as well. Other features are noticeable: for all curves, the energy is largest on the axis as a consequence of the focused beam. It decreases as the angle increases in the main part of the plume, and drops significantly at what corresponds to the beam half-angle. Interestingly, this abrupt change of slope happens at a larger angle for the cases $\dot{m}_a$ = 5 sccm and V_d = 250 V, indicating a larger divergence for these operating conditions. It is visible around θ = -40 ° for these two curves (cyan and red) and around θ = -35 ° for the other two.
The discharge voltage was varied from 200 to 400 V and the consequent variation of the most probable ion energy is plotted in Fig. 10. It is clear that the $\mathcal{E}_i$ varies linearly with V_d. This could mean that over this range, the voltage only affects the ion acceleration without fundamentally changing the behavior of the internal plasma discharge. Moreover, Fig. 10 includes measurements at multiple distances for each voltage. These points overlay, confirming that the ions are almost fully accelerated beyond z = 18.5 cm.
Finally, Fig. 11 exhibits how the IEDF changes with the angle. These distribution functions correspond to the data of the reference point represented in black in Fig. 9b. At every angle, the IEDF is composed of a single peak shifting towards lower energies as θ increases, at a rate that changes around θ = -35 °, as observed in Fig. 9b. Other published works reported RPA measurements showing similar IEDF shapes in CHT [2, 12, 31] with a single peak at energies corresponding to a large fraction of the discharge voltage. More complex IEDF are sometimes observed in traditional annular Hall thrusters [18] and in CHT [5], with multiple ion populations at low energies. Those slow ions are often identified as resulting from downstream ionization and charge exchange collisions. The thruster tested in [5] is very different from the CHT used in this work, in terms of channel dimensions and anode propellant flow rate. It also has a much weaker magnetic field. This could be an explanation for the appearance of slow ions.
For some points, the voltage on the first grid of the RPA was swept using a Keithley 2410 SMU to roughly estimate the local plasma potential to be accounted for in the calculation of the ion velocity according to Eq. (3). Taking the reference operating conditions as an example ($\dot{m}_a$ = 3.5 sccm, V_d = 300 V, I_{TC} = 1 A, I_{BC} = 1.7 A, with a CRP of -39 V), it was found that ϕ_{pl} = 3.75 V at z = 33.5 cm from the exit plane, and the calculated ion most probable velocity is v_i = 18.15 km.s^{-1}. This amounts for 86 % of the velocity that would be achieved by the ions if they were accelerated by the full discharge voltage, and it represents 93 % of the actual potential difference between the anode and the plasma at the probed location ($\Delta\phi = V_d - \phi_{pl}$ + CRP). This means that the potential drop in the plasma is quite efficiently used to accelerate the ions, but that the cathode seizes an important fraction of the voltage that does not contribute to the ion kinetic energy. The exhaust velocity could certainly be improved by coupling the thruster with a cathode of more appropriate dimensions for sub-ampere discharge currents, and by optimizing its operation (mass flow rate, heater and keeper power).

C. Faraday cup

1. Effect of input parameters

The ion current density was measured in the plume of the CHT between θ = -90 ° and θ = 90 ° (in some cases between θ = -90 ° and θ = 0 °), for several operating points of the thruster. The variation of three parameters, namely $\dot{m}_a$, V_d, and $\vec{B}$, is presented in Fig. 12. The values of the parameter varied are showed in the legend while the other conditions are the ones of the nominal case considered in the previous sections, i.e. V_d = 300 V, $\dot{m}_a$ = 3.5 sccm, I_{TC} = 1 A, and I_{BC} = 1.7 A, unless specified otherwise.
Figure 12a presents the variation of the anode mass flow rate. As expected, when $\dot{m}_a$ is increased, the larger neutral density in the channel enhances the ionization which results in a larger discharge current and a larger ion current density in the beam (Fig. 12a, top graph). This observation is consistent with the larger plasma density measured with the LP in the case $\dot{m}_a$ = 5 sccm (section V.A.1). This translates into a 40% improvement of the propellant utilization η_u as $\dot{m}_a$ is doubled (Fig. 12a, middle graph). At the largest mass flow, η_u reaches almost 100%, which confirms that the thruster can ionize very efficiently. Values of propellant utilization reported in literature for CHT often exceed unity [2, 5, 6], which is justified by the large fraction of multiply charged ions according to the authors. The presence of multiply charged ions is not assessed in this work, however, values of η_u larger than 1 were obtained for almost all the FC scans when the propellant utilization was computed using the anode mass flow rate. This seems unreasonable given the large ratio $\dot{m}_c/\dot{m}_a$. As a consequence the values of η_u displayed in Fig. 12 consider the total propellant flow rate

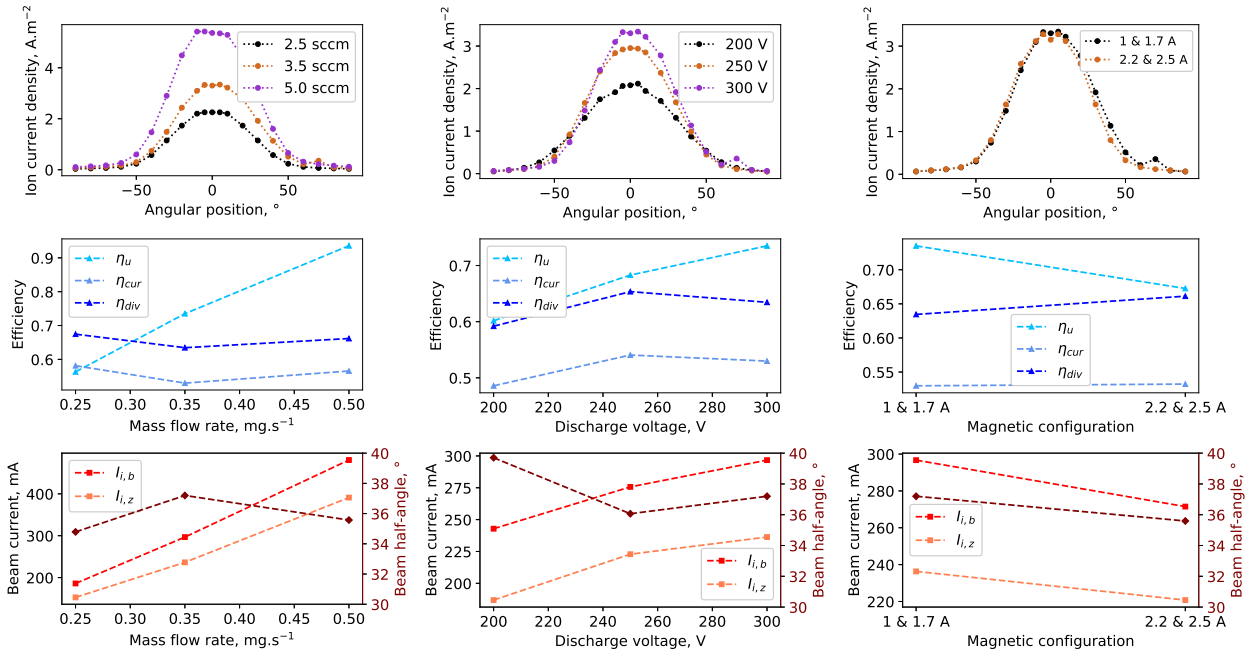

(a) Effect of the anode mass flow rate **(b) Effect of the discharge voltage** **(c) Effect of the magnetic field**

Fig. 12 Ion current density measured at z = 27 cm from the thruster (top row), computed propellant utilization η_u, current utilization η_{cur} and divergence efficiency η_{div} (middle row) and computed ion total current, ion axial current, and beam half-angle (bottom row)

$\dot{m}_p = \dot{m}_a + \dot{m}_c$. The divergence and current utilization appear to be only lightly affected by the anode flow rate over the range tested.

The effect of the discharge voltage is analyzed from the results in Fig. 12b. Similarly to the increase of $\dot{m}_a$, an increase of V_d appears to improve the propellant utilization efficiency (Fig. 12b, middle graph), certainly due to the greater energy provided by the electric field to the electrons that is used for ionization. As a consequence, the discharge current and the beam current are both increase with V_d (Fig. 12b, top and bottom graphs) . The effect of V_d on the divergence and on the current utilization is non-trivial and the trends suggest that there might be an intermediate voltage that maximizes those efficiencies, but more data is needed for this to be confirmed. However, given that the impact of V_d on η_u is much more important than the impact on η_{cur} and η_{div}, the overall performance is expected to be better with a larger voltage in this range.

Eventually, FC scans of the two magnetic field configurations are displayed in Fig. 12c. The most visible effect of the field is the decrease in the propellant utilization, although it represents a change of about 5 % only. The current density scans overlay at negative angles, and the difference between the two curves at positive angles is thought to be due to measurement errors, as the beam current was varying during the test. This will be explained in section V.C.2. Thus, it seems that the two sets of coils current tested do not affect much the beam properties measured with the FC, the same thing is visible in the LP results.

2. Measurement conditions

Some elements added uncertainty to the ion density measurements such as the difficulty of determining the right collector bias to use, or the fact that some flaw in the external fluid assembly caused low frequency oscillations of the mass flow rates of xenon injected through the anode and cathode. This induced oscillations of the discharge current and beam current that affected the results. Even though the FC current was averaged over multiple acquisitions, this is still visible in some points. Note that this concerns only the FC data. Finally, the cathode was not always working in the same way. In the FC cup, the cathode heating power was kept constant, around P_h = 80 W, for all the cases presented in Fig. 12. However, the CRP varied between those measurements, sometimes by several tens of volts. Thus the reader should bear in mind that the curves are only partially comparable as some changes in the performance might be in part

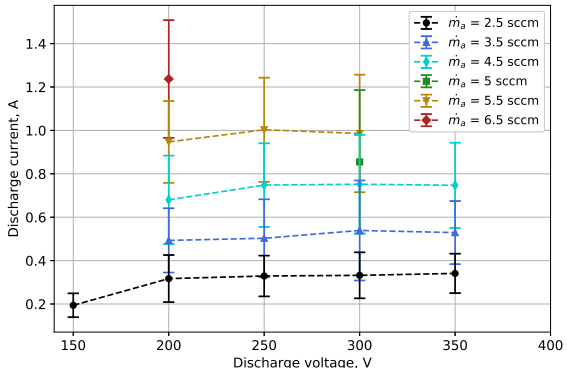

Fig. 13 Variation of the discharge current with the discharge voltage, for different anode mass flow rates. The error bars indicate the current oscillation amplitude.

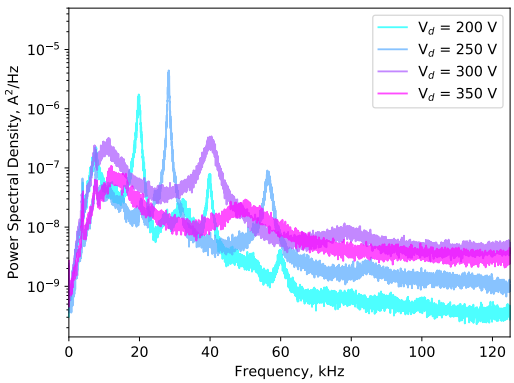

Fig. 14 Evolution of the discharge current PSD with discharge voltage, for $\dot{m}_a$ = 3.5 sccm

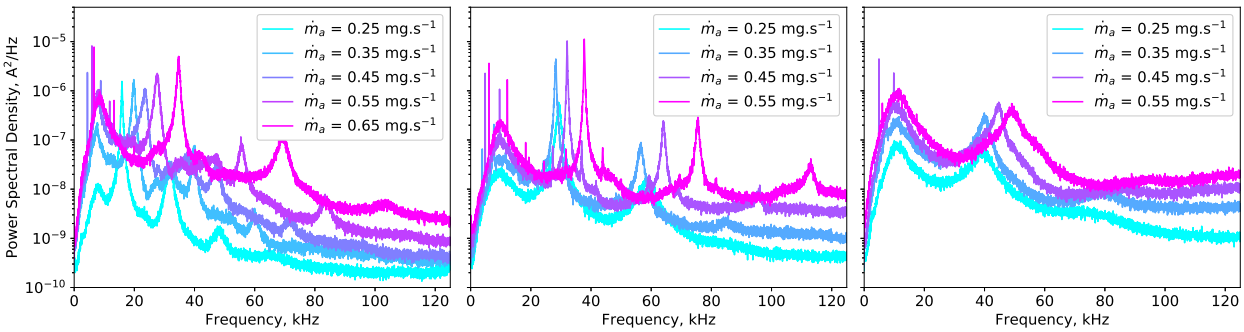

(a) V_d = 200 V **(b) V_d = 250 V** **(c) V_d = 300 V**

Fig. 15 Evolution of the discharge current PSD with anode mass flow rate for three different discharge voltages

related to the different CRP. The CRP was fixed (around -39 V) by adjusting P_h during the LP and RPA measurements. Instead during the FC scans, for the reference conditions, the CRP was -101 V.

D. Current probe

The variation of the discharge current with the discharge voltage and mass flow rate is represented in Fig. 13. The time signal measured with the current probe was processed to obtain the RMS value of the current and the peak-to-peak oscillation amplitude, which are plotted in this graph. The discharge current tends to increase both with $\dot{m}_a$ and V_d, but it is clearly much more sensitive to changes in the propellant flow rate than to changes in the voltage. The absolute value of the oscillation amplitude increases with the mass flow, but the ratio of the oscillation amplitude to the RMS current does not show any clear trend with the variation of V_d and $\dot{m}_a$.

The PSD of the discharge current can be seen in Fig. 14 for four different anode voltages, at an anode flow rate of 3.5 sccm, in the magnetic configuration corresponding to the reference conditions. In a similar way, each graph in Fig. 15 compares the PSD of I_d at different mass flow rates, while V_d and $\vec{B}$ are fixed. Firstly, on all these plots, a first peak at low frequency ($\sim$ 7 - 11 kHz) is visible as well as another peak at higher frequency ($\geq$ 15 kHz). Other major peaks at higher frequencies were identified to be harmonics of the latter.

In Fig. 14, one can see that frequency of the first peak is is sligthly increased by the increment of V_d. Instead, Fig. 15 shows that this frequency is almost unaffected by changes of anode mass flow rate.

Instead, the second peak is significantly damped and shifted towards higher frequency as the voltage is raised (Fig. 14), which, additionally, seems to suppress its harmonic frequencies. This is quite similar to the HET oscillatory behaviors reported in [32]. Varying $\dot{m}_a$ also has an effect on this second peak, a larger mass flow induces a greater amplitude of this oscillation, and a greater frequency as well, no matter the anode voltage (Fig. 15).

Finally, another remark can be done about the fact that the first peak is the highest one at V_d = 300 V (Fig. 15c) while it has less power than the second peak in the 200 V and 250 V cases (Fig. 15a and 15b). Since the first and second peaks appear to vary differently with the discharge parameters, they are most likely the consequence of two different mechanisms occurring in the plasma. This suggests that modifications of the thruster input parameters can determine which is the dominant oscillatory mode. In fact, some research works focused on oscillations in Hall thruster discharges suggest that peaks in this frequency range could be associated to the rotating spokes and breathing mode oscillations [33, 34]. It should be mentioned that some $\sim$ 3.3 kHz and 15 - 35 kHz azimuthal oscillations and 11 - 14 kHz breathing mode were observed in a similar thruster [35, 36]. Further analysis of the discharge properties in the CHT is necessary to clearly identify the origins of these oscillations.

VI. Conclusions

The test campaign summarized in this work focused on the characterization of the operating envelope and measurement of the plasma parameters in the far-field of a Cylindrical Hall Thruster prototype coupled with a LaB_6 hollow cathode. The thruster was operated between 30 - 300 W of discharge power, which was achieved by varying the discharge voltage over the range 150 - 350 V and the propellant mass flow rate injected through the anode over the range 0.25 - 0.65 mg.s^{-1}. The behavior of the device was analyzed during and after the tests with the perspective of future design improvements. Plasma properties such as the electron temperature, plasma density and electric potential were assessed in the axial-azimuthal plane of the thruster plume using a Langmuir Probe. The variation of these properties along the thruster axis was compared for four operating conditions that included different magnetic topologies, discharge voltages and anode mass flow rates. The Langmuir Probe data were also used to characterize electron thermodynamics in the expelled plasma. Measurements of the properties of the ions were performed as well. The ion energy was evaluated with a Retarding Potential Analyzer that measured the Ion Energy Distribution Function at various axial and angular positions in the beam. This allowed for estimating the ion axial velocity. Ultimately, the ion current density in the beam was measured and provided information about the propellant utilization, current utilization and beam divergence. Furthermore, measurements of the time evolution of the discharge current were used to study the effect of two input parameters, namely the anode voltage and flow rate, on the oscillations occurring in the plasma discharge. Some major observations from these results included the positive effect of increasing the mass flow rate on the ionization, which consequently increased the plasma density, propellant utilization, currents and some oscillation frequencies. However, it had generally negative effects on the ion acceleration. Changing the magnetic field appeared to have little impact on the discharge properties while variations of the anode voltage bias had consequences on all the magnitudes measured, with more efficient operation at larger voltages. Eventually, the xenon flow rate and anode voltage were shown to alter the amplitude, complexity and frequency of the discharge current oscillations, which seemed to be mainly composed of two different modes. The characterization of this CHT prototype showed rather expectable and promising results. It also highlighted many possibilities of improvements of the design and operation. Future experimental activities on this device shall include the use of non-intrusive diagnostics inside the thruster channel, and testing with other types of neutralizers.

Acknowledgments

This work has been supported by the PROMETEO project funded by the Comunidad de Madrid under the grant number Y2018/NMT4750, and by the project ESPEOS funded by the Spanish Government under the grant number PID2019-108034RB-I00. The authors would like to thank C. Royer and U. Weller for their help in setting up the experimental campaign.

References

[1] Raitses, Y., Dorf, L. A., Litvak, A. A., and Fisch, N. J., "Plume Reduction in Segmented Electrode Hall Thruster," *Journal of Applied Physics*, Vol. 88, No. 3, 2000, pp. 1263–1270. https://doi.org/10.1063/1.373813.

[2] Smirnov, A., Raitses, Y., and Fisch, N. J., "Experimental and Theoretical Studies of Cylindrical Hall Thrusters," *Physics of Plasmas*, Vol. 14, No. 5, 2006, p. 057106. https://doi.org/10.1063/1.2718522.

[3] Ikeda, Togawa, Nishida, Tahara, and Watanabe, "Research and Development of Very Low Power Cylindrical Hall Thrusters for Nano-Satellites," *32nd International Electric Propulsion Conference*, Wiesbaden • Germany, 2011.

[4] Ikeda, T., Togawa, K., Tahara, H., and Watanabe, Y., "Performance Characteristics of Very Low Power Cylindrical Hall Thrusters for the Nano-Satellite "PROITERES-3"," *Vacuum*, Vol. 88, 2013, pp. 63–69. https://doi.org/10.1016/j.vacuum.2012.04.012.

[5] Shirasaki, A., and Tahara, H., "Operational Characteristics and Plasma Measurements in Cylindrical Hall Thrusters," *Journal of Applied Physics*, Vol. 101, No. 7, 2007, p. 073307. https://doi.org/10.1063/1.2720093.

[6] Gao, Y., Liu, H., Hu, P., Huang, H., and Yu, D., "The Effect of Magnetic Field near the Anode on Cylindrical Hall Thruster," *Plasma Sources Science and Technology*, Vol. 25, No. 3, 2016, p. 035011. https://doi.org/10.1088/0963-0252/25/3/035011.

[7] Seo, M., Lee, J., Seon, J., June Lee, H., and Choe, W., "Radial Scale Effect on the Performance of Low-Power Cylindrical Hall Plasma Thrusters," *Applied Physics Letters*, Vol. 103, No. 13, 2013, p. 133501. https://doi.org/10.1063/1.4820774.

[8] Lee, J., Seo, M., Seon, J., June Lee, H., and Choe, W., "Performance Characteristics According to the Channel Length and Magnetic Fields of Cylindrical Hall Thrusters," *Applied Physics Letters*, Vol. 99, No. 13, 2011, p. 131505. https://doi.org/10.1063/1.3643435.

[9] Smirnov, A., Raitses, Y., and Fisch, N., "Plasma Measurements of a 100 W Cylindrical Hall Thruster," *39th AIAA/ASME/SAE/ASEE Joint Propulsion Conference and Exhibit*, American Institute of Aeronautics and Astronautics, Huntsville, Alabama, 2003. https://doi.org/10.2514/6.2003-5000.

[10] Raitses, Y., Merino, E., and Fisch, N. J., "Cylindrical Hall Thrusters with Permanent Magnets," *Journal of Applied Physics*, 2010, p. 10.

[11] Raitses, Y., Smirnov, A., Granstedt, E., and Fisch, N., "Optimization of Cylindrical Hall Thrusters," *43rd AIAA/ASME/SAE/ASEE Joint Propulsion Conference & Exhibit*, American Institute of Aeronautics and Astronautics, Cincinnati, OH, 2007. https://doi.org/10.2514/6.2007-5204.

[12] Kim, H., Choe, W., Lim, Y., Lee, S., and Park, S., "Magnetic Field Configurations on Thruster Performance in Accordance with Ion Beam Characteristics in Cylindrical Hall Thruster Plasmas," *Applied Physics Letters*, Vol. 110, No. 11, 2017, p. 114101. https://doi.org/10.1063/1.4978532.

[13] Perrotin, T., Domínguez-Vázquez, A., Navarro-Cavallé, J., Fajardo, P., and Ahedo, E., "Design and Preliminary Study of a 200W Cylindrical Hall Thruster," *Space Propulsion Conference*, Estoril, Portugal, 2021, p. 11.

[14] Garrigues, Santhosh, Grimaud, and Mazouffre, "Operation of a Low Power Hall Thruster with a Shielded Magnetically Configuration," *36th International Electric Propulsion Conference*, University of Vienna • Vienna, Austria, 2019.

[15] Chen, F. F., "Langmuir Probes in RF Plasma: Surprising Validity of OML Theory," *Plasma Sources Science and Technology*, Vol. 18, No. 3, 2009, p. 035012. https://doi.org/10.1088/0963-0252/18/3/035012.

[16] Lobbia, R. B., and Beal, B. E., "Recommended Practice for Use of Langmuir Probes in Electric Propulsion Testing," *Journal of Propulsion and Power*, Vol. 33, No. 3, 2017, pp. 566–581. https://doi.org/10.2514/1.B35531.

[17] Gulbrandsen, N., Fredriksen, Å., Carr, J., and Scime, E., "A Comparison of Ion Beam Measurements by Retarding Field Energy Analyzer and Laser Induced Fluorescence in Helicon Plasma Devices," *Physics of Plasmas*, Vol. 22, No. 3, 2015, p. 033505. https://doi.org/10.1063/1.4913990.

[18] Hallouin, T., and Mazouffre, S., "Far-Field Plume Characterization of a 100-W Class Hall Thruster," *Aerospace*, Vol. 7, No. 5, 2020, p. 58. https://doi.org/10.3390/aerospace7050058.

[19] Hugonnaud, V., and Mazouffre, S., "Optimization of a Faraday Cup Collimator for Electric Propulsion Device Beam Study: Case of a Hall Thruster," *Applied Sciences*, Vol. 11, No. 5, 2021, p. 2419. https://doi.org/10.3390/app11052419.

[20] Brown, D. L., Walker, M. L. R., Szabo, J., Huang, W., and Foster, J. E., "Recommended Practice for Use of Faraday Probes in Electric Propulsion Testing," *Journal of Propulsion and Power*, Vol. 33, No. 3, 2017, pp. 582–613. https://doi.org/10.2514/1.B35696.

[21] Hugonnaud, V., Mazouffre, S., Krejci, D., Scharlemann, C., and Seifert, B., "Faraday Cup Design for Low Power Electric Thrusters," *Space Propulsion Conference*, Estoril, Portugal, 2021, p. 13.

[22] Pigeon, C., "Development of a Miniature Low Power Hall Thruster for Microsatellites," Ph.D. thesis, 2017.

[23] Giono, G., Gudmundsson, J. T., Ivchenko, N., Mazouffre, S., Dannenmayer, K., Loubère, D., Popelier, L., Merino, M., and Olentšenko, G., "Non-Maxwellian Electron Energy Probability Functions in the Plume of a SPT-100 Hall Thruster," *Plasma Sources Science and Technology*, Vol. 27, No. 1, 2017, p. 015006. https://doi.org/10.1088/1361-6595/aaa06b.

[24] Dannenmayer, K., Kudrna, P., Tichý, M., and Mazouffre, S., "Measurement of Plasma Parameters in the Far-Field Plume of a Hall Effect Thruster," *Plasma Sources Science and Technology*, Vol. 20, No. 6, 2011, p. 065012. https://doi.org/10.1088/0963-0252/20/6/065012.

[25] Diamant, K., Pollard, J., Raitses, Y., and Fisch, N., "Low Power Cylindrical Hall Thruster Performance and Plume Properties," *44th AIAA/ASME/SAE/ASEE Joint Propulsion Conference & Exhibit*, American Institute of Aeronautics and Astronautics, Hartford, CT, 2008. https://doi.org/10.2514/6.2008-4998.

[26] Dannenmayer, K., and Mazouffre, S., "Electron Flow Properties in the Far-Field Plume of a Hall Thruster," *Plasma Sources Science and Technology*, Vol. 22, No. 3, 2013, p. 035004. https://doi.org/10.1088/0963-0252/22/3/035004.

[27] Nicolaou, G., Livadiotis, G., and Wicks, R. T., "On the Calculation of the Effective Polytropic Index in Space Plasmas," *Entropy*, Vol. 21, No. 10, 2019, p. 997. https://doi.org/10.3390/e21100997.

[28] Livadiotis, G., and Nicolaou, G., "Relationship between Polytropic Index and Temperature Anisotropy in Space Plasmas," *The Astrophysical Journal*, Vol. 909, No. 2, 2021, p. 127. https://doi.org/10.3847/1538-4357/abda44.

[29] Vinci, A. E., Delavière–Delion, Q., and Mazouffre, S., "Electron Thermodynamics along Magnetic Nozzle Lines in a Helicon Plasma," *Journal of Electric Propulsion*, Vol. 1, No. 1, 2022, p. 4. https://doi.org/10.1007/s44205-022-00003-0.

[30] Kim, J. Y., Go, G., Hwang, Y. S., and Chung, K.-J., "Dependence of the Polytropic Index of Plasma on Magnetic Field," *New Journal of Physics*, Vol. 23, No. 5, 2021, p. 052001. https://doi.org/10.1088/1367-2630/abfab1.

[31] Seo, M., Lee, J., Seon, J., June Lee, H., and Choe, W., "Radial Scale Effect on the Performance of Low-Power Cylindrical Hall Plasma Thrusters," *Applied Physics Letters*, Vol. 103, No. 13, 2013, p. 133501. https://doi.org/10.1063/1.4820774.

[32] Lobbia, R. B., and Gallimore, A. D., "Two-Dimensional Time-resolved Breathing Mode Plasma Fluctuation Variation with Hall Thruster Discharge Settings," *31st International Electric Propulsion Conference*, University of Michigan, 2009.

[33] Choueiri, E. Y., "Plasma Oscillations in Hall Thrusters," *Physics of Plasmas*, Vol. 8, No. 4, 2001, p. 1411. https://doi.org/10.1063/1.1354644.

[34] Boeuf, J.-P., "Tutorial: Physics and Modeling of Hall Thrusters," *Journal of Applied Physics*, Vol. 121, No. 1, 2017, p. 011101. https://doi.org/10.1063/1.4972269.

[35] Ellison, C. L., Raitses, Y., and Fisch, N. J., "Cross-Field Electron Transport Induced by a Rotating Spoke in a Cylindrical Hall Thruster," *Physics of Plasmas*, Vol. 19, No. 1, 2012, p. 013503. https://doi.org/10.1063/1.3671920.

[36] Polzin, K. A., Sooby, E. S., Raitses, Y., Merino, E., and Fisch, N. J., "Discharge Oscillations in a Permanent Magnet Cylindrical Hall-Effect Thruster," *31st International Electric Propulsion Conference*, 2009.